https://doi.org/10.1007/s44205-025-00123-3

Journal of Electric Propulsion

RESEARCH Open Access

# Development and characterization of the ALFVEN thruster

Yung-An Chan[1*], Kazunori Takahashi[2], Martin Grabe[1] and Christopher Geile[1]

*Correspondence:
yung-an.chan@dlr.de

[1] Institute of Aerodynamics and Flow Technology, German Aerospace Center, Bunsenstraße 10, 37073 Göttingen, Germany
[2] Department of Electrical Engineering, Tohoku University, 6 - 6- 05, Aramaki-Aza-Aoba, Aoba-Ku, Sendai 980 - 8579, Japan

## Abstract

The Advanced Linear Field Vector Excitation Network (ALFVEN) thruster represents a novel RF plasma propulsion system developed to enhance the coupling efficiency of electromagnetic waves to plasma, particularly in low-power conditions. This study presents the design, development, and experimental characterization of the ALFVEN-4050, an RF thruster utilizing a resonant network to generate a linear-polarized electromagnetic field in the transverse direction of the thruster's discharge chamber. The innovations of ALFVEN- 4050 include utilizing a square-loop antenna array and the orthogonal coupling of the transverse electromagnetic field and uniform magnetic flux across the discharge chamber, enabling efficient plasma generation. Experimental results using argon and krypton propellants demonstrate promising ignition capabilities for low gas flow rate and stable impedance matching. The ALFVEN thruster's performance highlights its potential to overcome challenges in low-power RF plasma thrusters, such as low mass utilization efficiency, paving the way for advanced EP concepts for applications with alternative propellants.

**Keywords:** Electric propulsion, Radio-frequency, Resonant antenna

## Introduction

Neutralizer-free or electroless thruster concepts, such as a helicon plasma thruster (HPT) and an electron-cyclotron-resonance (ECR) thruster, rely on the heating mechanisms with electromagnetic fields, which provide plasma generation for propulsive purposes [1]. Eliminating electrode exposure to the plasma provides superior compatibility with alternative propellants such as water or Iodine [2, 3], and mitigate electrode degradation caused by ion bombardment and chemical reactions. Thus, the EP concepts based on these technologies can offer promising advantages for new space applications.

Recently, the thrust efficiency of the HPT has been significantly improved to nearly 30% [4], mainly attributed to improving the magnetic confinement in the source and the plasma-gas interaction [5], increasing the operation power, and understanding the plasma dynamics in magnetic nozzles [6]. However, the low-power HPT, i.e., few-hundred-watt class [7] and sub-hundred-watt class [3], remains relatively low in performance. Literature also suggests that the significant loss is mass utilization efficiency, which is driven by the ionization cost and is related to the species'ionization energy, power coupling efficiency, and energy loss to the thruster wall [2, 8]. Attempts to reduce wall loss have also been implemented using the strong magnetic field and the cusp-type fields for plasma confinement with a high-power helicon source [8]. However, the more substantial field could potentially cause issues with plasma detachment [9].

An alternative approach to improving mass utilization efficiency is to improve the power coupling between the antenna and plasma, which is particularly important when the thruster is operated in low-power conditions, and the propellant has a low mass flow rate. Furthermore, the direct ignition of the discharge by the antenna is crucial to minimize the system size of the EP device. Accordingly, the design of the plasma antenna and the coupling mechanism becomes crucial for the low-power electrodeless thruster. Advanced-Linear Field Vector Excitation Network, aka ALFVEN, is proposed to optimize radio-frequency (RF) power transmission.

ALFVEN is a resonant network that aims to generate a linear-polarized oscillating electromagnetic field across the whole discharge chamber in the transverse direction axis with a radio-frequency wave. Unlike the known HPT or ICP thruster, which utilizes an inductive component as a plasma antenna in series with the power unit, ALFVEN is more similar to the function of the birdcage antenna, i.e., an antenna made of a parallel resonant circuit. More details on the fundamental principle of ALFVEN and the birdcage antenna can be found in Ref. [10–12] Yet, ALFVEN enables linear scaling of geometry, design impedance, and operating frequency. Since ALFVEN inherited the feature of a resonant network, the total equivalent resistance could be increased significantly, enabling lower current flowing in the circuit. Thus, the power loss in the impedance-matching circuit due to the ohmic heating could be minimized. Resonant circuits used for plasma generation have demonstrated promising power transmission efficiency and significant plasma density enhancement. [13, 14]

The second feature of ALFVEN is the linear-polarized oscillating electromagnetic field in the transverse direction of the discharge chamber. One could enable the optimization of the $\widetilde{E} \times \overrightarrow{B}_0$ condition from the antenna to the plasma by carefully designing an axisymmetric magnetic field topography. This offers a mechanism similar to plasma generation, as the ECR thruster, but operates in a lower frequency domain. This feature enables minimizing power loss in the transmission line, utilizing high-efficiency DC-RF power conversion, and releasing the tolerance requirement for circuit and antenna manufacturing. A preliminary experimental observation of the ECR in the 13.56 MHz magnetic enhanced plasma source has pointed out the possibility of utilizing the RF wave to trigger the ECR effect [15].

Nevertheless, whether the thruster design with the ALFVEN concept can be categorized as a type of HPT or ECR thruster remains an open question due to the need for further experimental verification of the wave propagation and dispersion in plasma.

This paper presents an RF thruster demonstrator based on ALFVEN technology, i.e., ALFVEN- 4050. The resonant frequency is designed around 40 MHz and has an impedance of 50 Ω. The discussion focuses on the discharge capability and the impedance variation resulting from the presence of plasma, accompanied by the measurement of plasma properties.

## ALFVEN thruster design

The concept illustration and the picture of the ALFVEN thruster are shown in Fig. 1, which consists of an RF plasma source and magnetic optics. An advanced antenna concept is proposed to improve the power coupling between plasma and antenna. The antenna comprises a square-loop array (SLA) that is azimuthally distributed around the cylindrical quartz tube, which serves as the plasma discharge chamber. The antenna aims to generate a uniform, transversely oscillating electromagnetic field within the discharge region, providing a function similar to that of the cylindrical birdcage antenna for plasma generation. [10, 11] Beyond the scope of the birdcage antenna, the SLA offers greater flexibility in the engineering design of the resonant antenna at approximately the same antenna dimension, such as antenna impedance and operating frequency by further detailing the antenna design, providing high adaptability to the specification of the RF power unit. The thruster is isolated from the facility's ground and the RF power circuit by using an inner/outer DC block, which still allows the HF power transmission. This implementation enables the measurement of the thruster potential during operation.

The ALFVEN- 4050 has a dimension of 118mm × 118 mm × 86.5 mm, with a discharge chamber of 40 mm inner diameter and a length of 90 mm. The thruster is electrically isolated from the ground using PEEK as the supporting structure and a DC isolator on the power feeding line. A quartz tube is extended from the thruster exit to the end of the quartz tube cape, which allows the plasma in the discharge chamber to be isolated to the surrounding structure but only exposed to the distributed plate. The propellant is injected into a small pre-chamber encapsulated by a showerhead distributing plate, enabling a uniform gas distribution across the section of the discharge chamber. In addition, the distributed plate is in contact with the plasma and the thruster body, creating an equal potential between the plasma and the thruster body. One can roughly determine the plasma potential in the discharge chamber by measuring the thruster potential from the thruster body.

The design of magnetic optics is indicated in Fig. 1, which is comprised of four sets of NdFeB permanent magnets and two pieces of soft iron plate to guide magnetic flux to the discharge chamber. The goal is to achieve a uniform magnetic flux distributed across the discharge chamber.

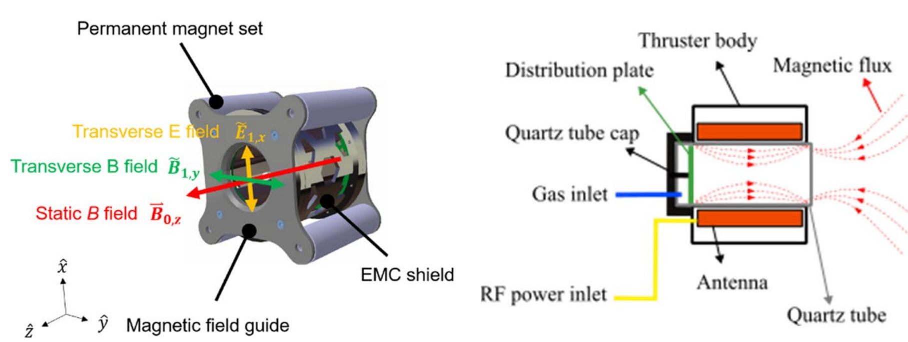


**Fig. 1** Concept illustration of ALFVEN thruster: Thruster CAD model with the applied magnetic field $\vec{B}_{0z}$ and oscillating electromagnetic field $\widetilde{B}_{1,y}$ and $\widetilde{E}_{1,x}$ (left), and the cross-section view of the thruster assembly (right)

**Antenna design and working principle**

An electric schematic of the SLA of the ALFVEN- 4050 can be found in Fig. 2, which is similar to the circuit of the cylindrical birdcage antenna. [10] The idea is to generate a sinusoidal current distribution over the cylindrical surface enclosed by the legs of the antenna, which is able to formulate a linear B-field in the transversal direction across the volume enclosed by the legs. Two rings are located at the end of each leg, and the capacitors are between them to adjust the resonance frequency of the SLA. By expanding the circuit into planar form, the schematic can be represented as an infinite ladder circuit, as shown in Fig. 3. The $Z_1$, $Z_2$, and $Z_{\mathrm{Load}}$ represent the equivalent impedance of the leg, ring, and the equivalent impedance of the SLA as load. The equation for the $Z_{\mathrm{Load}}$, $Z_1$, and $Z_2$ are beyond the scope of this paper. However, a detailed derivation for $Z_{\mathrm{Load}}$, $Z_1$, and $Z_2$ can be found in Ref. [16].

The $i_{\mathrm{leg}}$ represents the current flowing in the leg of the SLA, which is designed purposely to provide a standing wave propagation within the ladder circuit. Since the circuit of SLA is designed to resonant at a single frequency (i.e., $Z_{\mathrm{Load}} = 50\Omega$), the reflective power from the RF power system can be minimized, indicating the ideal power transfers from the RF source to the antenna circuit.

The circuit component for the ALFVEN- 4050 can be found in the following ladder circuit schematics, shown in Fig. 4. The circuit used for ALFVEN is a high-pass circuit.

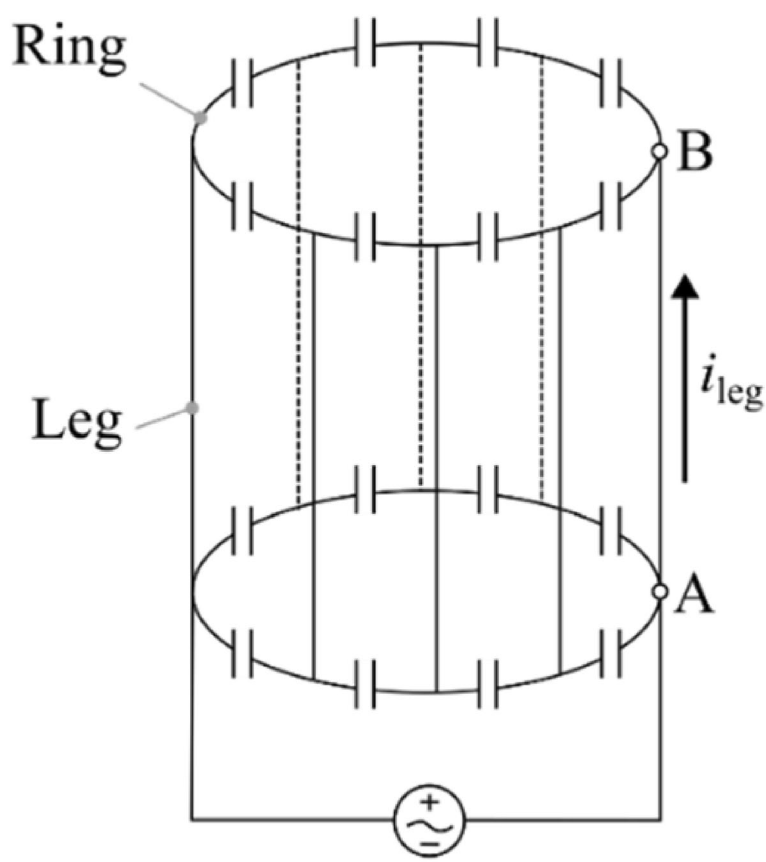


**Fig. 2** Illustration of the electric schematic of the ALFVEN- 4050 antenna

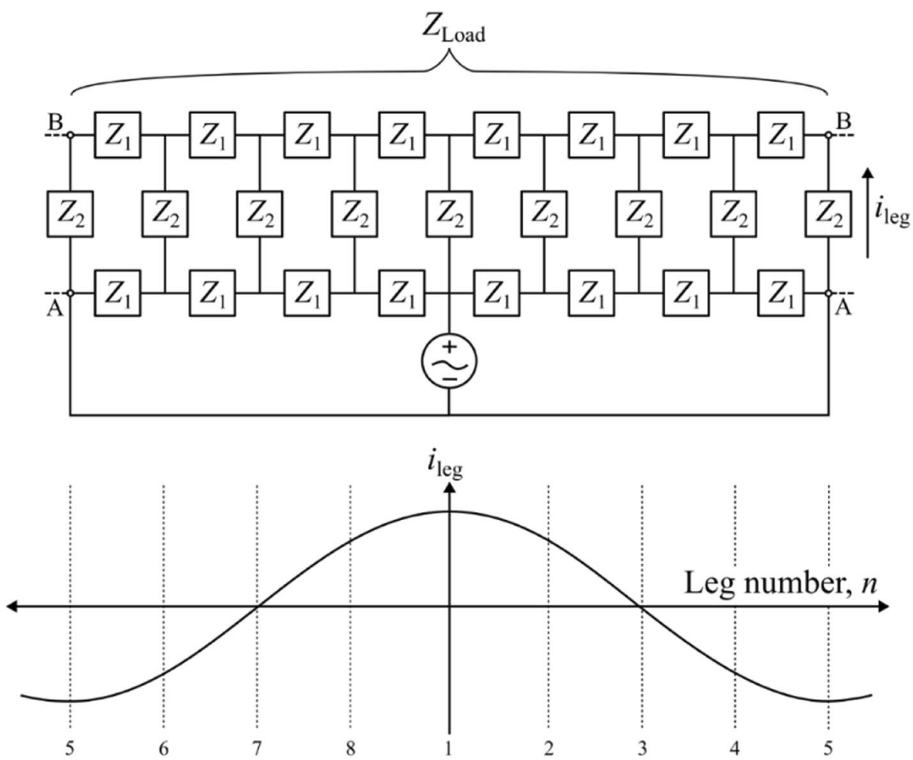


**Fig. 3** Concept illustration of the infinite-loop ladder circuit for ALFVEN- 4050

The $Z_1$ is composed of a series circuit including a capacitance ($C_{\text{ring}}$), resistance ($R_{\text{ring}}$), and the mutual inductance on the ring ($M_{\text{ring}}$), while the $Z_2$ is composed of a self-inductance of the leg ($L_{\text{leg}}$) and the resistance ($R_{\text{leg}}$). Therefore, the impedance of the ring and leg can be written as $Z_1 = R_{\text{ring}} + 1/(j\omega C_{\text{ring}}) + j\omega L_{\text{ring}}$ and $Z_2 = R_{\text{leg}} + j\omega L_{\text{leg}}$, respectively. The $M_{\text{ring}}$ is strongly affected by the geometry, the conductive parts' arrangement, and the RF excitation frequency to the antenna. The detailed calculation for the $M_{\text{ring}}$ is beyond the scope of this work. A 3D simulation for the SLA's overall impedance and the resonant frequency is more accurate and representative of the $Z_{\text{load}}$, which is shown in the next subsection (Fig. 5).

#### Antenna characteristics

The full-scale SLA of the ALFVEN- 4050 is designed with COMSOL HF module. The simulation is performed in the frequency domain from 30 to 55 MHz with a 0.1 MHz interval resolution. The material used for the simulation is selected from the COMSOL database according to the material used in the antenna. COMSOL automatically builds the mesh with the maximum element size of the simulation set at 3 mm for the shielding and 1 mm for the antenna structure, which is < 0.05% and < 1.83% than the simulated wavelength, respectively. The conductor surfaces are considered perfect electric conductors, which is reasonable due to the properties of the selected material. The properties of lump elements used in the antenna, i.e., capacitors, provide the equivalent series resistance and inductance at 40 MHz, were also taken into consideration. The input of the electromagnetic wave starts from a 50 Ω N-type connector to propagate through the antenna.

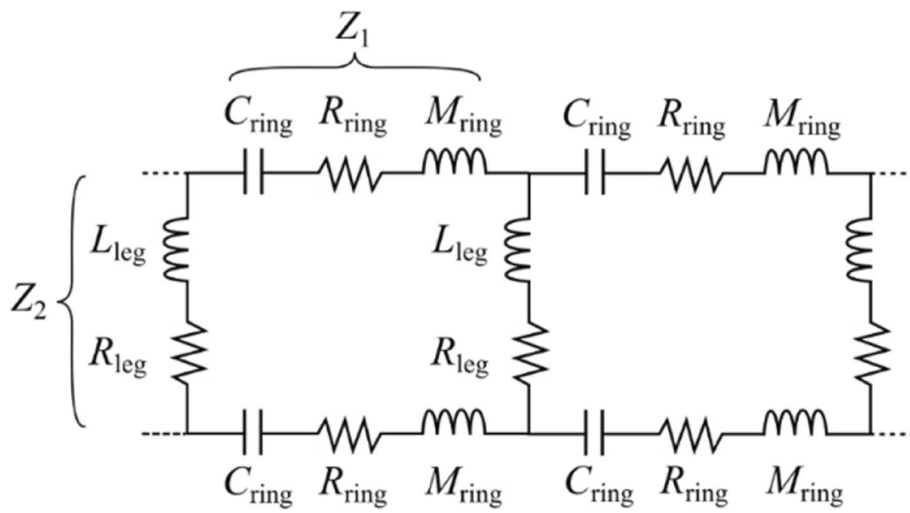


**Fig. 4** Electrical components and equivalent circuit of the SLA in ALFVEN- 4050

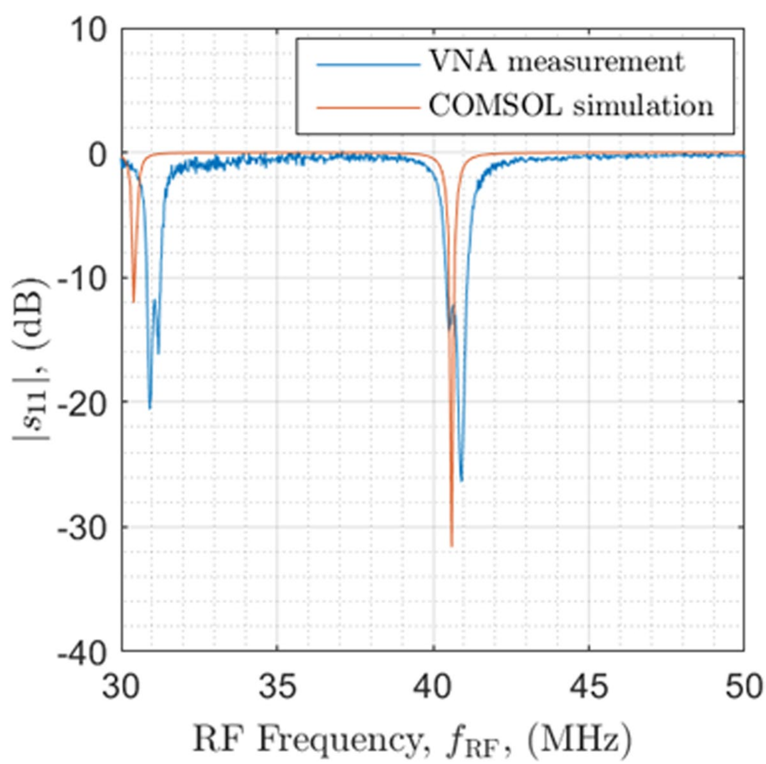


**Fig. 5** Simulated and measured $s_{11}$ parameter of the ALFVEN- 4050 antenna

The simulated $s_{11}$ parameter is shown in Fig. 5, together with the Vector Network Analyzer (VNA) measurement for ALFVEN- 4050 assembly. The VNA used for the calibration is Rigol RSA5065 N with calibration kit RIGOL CK106 A. The scanning frequency is from 30 to 50 MHz with a resolution of 5 kHz and 1000 samples averaging at each scanning frequency. The systematic uncertainty of the measurement is $< \pm 2.5$ ppm. Both spectrum profiles demonstrate consistent characteristics of SLA dual-band resonant frequency. The COMSOL simulation derived the $|s_{11}| = -31.5$ dB at the resonant frequency $f_{\mathrm{res}} = 40.6$ MHz. In contrast, the VNA measurement derived $|s_{11}| = -26.2$ dB at $f_{\mathrm{res}} = 40.82$ MHz $\cdot$ The resulting frequency shift could be derived from the deviation of the material properties from the perfect conductor, assembly tolerance, and the capacitors'uncertainty for achieving the resonance circuit. Among the possible discrepancies, the most probable cause is the uncertainty of the capacitor, which could have a 2% deviation from the central capacitance values.

### Magnetic field topography

A comparison of the COMSOL simulation of magnetic field topography and the 2D measurement across the discharge chamber's axial section is shown in Fig. 6. The magnetic flux at the position z$= -50$ mm is approximately 142 G$\pm$ 1.5 G. In addition, the magnetic flux diverges around the exit of the discharge chamber, which can partially serve as a magnetic nozzle. The field is uniformly distributed across the cross-section of the discharge chamber.

### Power supplying system

Figure 7 summarizes the architecture of the power-supplying system used for ALFVEN-4050 in a block diagram. The RF power supply is controlled by a Field Programmable Gate Arrays (FPGA) close-loop system, which monitors the power output and automatically tunes the signal frequency to maintain a constant net RF power given by $P_{\mathrm{f}} - P_{\mathrm{r}}$, where $P_{\mathrm{f}}$ and $P_{\mathrm{r}}$ are the forwarded and reflected powers, respectively. The FPGA system controls the voltage-controlled oscillator (VCO). An RF signal generated from the VCO is then sent to a voltage variable attenuator (VVA), which serves as an output power controller for the RF power amplifier. The amplifier is a class AB type with an operating

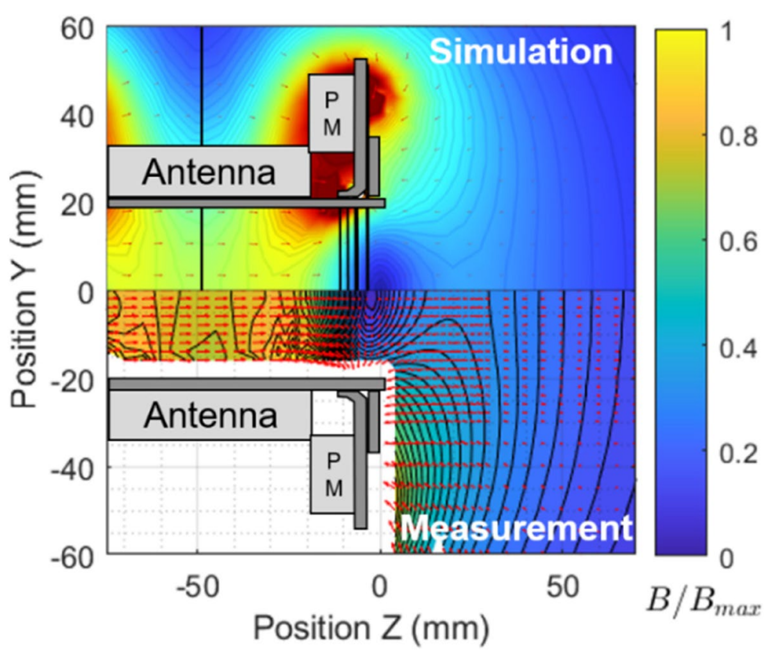


**Fig. 6** Comparison of 3D magnetic field simulation and 2D experimental measurement with Hall probe for ALFVEN- 4050

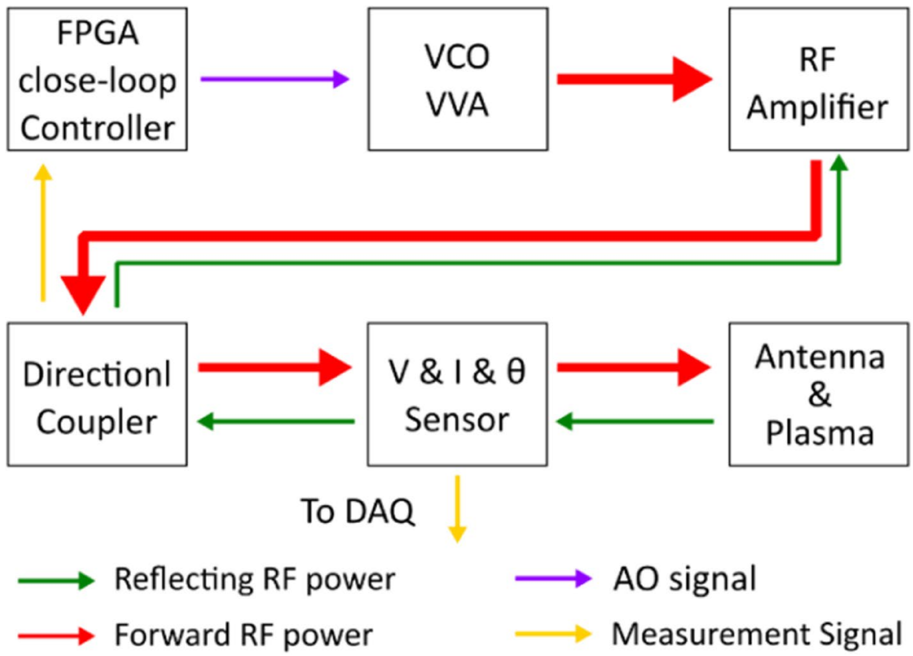


**Fig. 7** Power unit and transmission line architecture for ALFVEN- 4050 tested in Mega-HPT at Tohoku University, Japan

frequency at 40 ± 3MHz and output power up to 500 W at an impedance of 50 Ω. The output power is delivered through an RF bi-directional coupler, which converts the RF forward and reflected power into DC voltage for the FPGA to conduct close-loop auto-tuning processes on the frequency to maintain the net power output. Details of the RF power supply can be found in Ref. [17].

The frequency auto-matching function is disabled during an experiment to measure the circuit properties'variation when plasma is present. A commercial RF measurement device, known as Octiv Poly 2.0 from Impedans GmbH, is implemented between the power supply and ALFVEN to monitor the real-time variation of in-line voltage, current, and impedance of the RF power circuit when the plasma is in the discharge chamber. Since the antenna is with $Z_{\text{Load}} = 50\Omega$, the antenna provides excellent performance for plasma ignition. However, one has to pay attention to the fact that the load impedance could become more deviated from the matching condition (i.e. $Z_{\text{Load}} = 50\Omega$) as the input power increases. Accordingly, the experiment is carefully controlled within a specific power range to avoid damaging the RF power system or load.

## Test facility and experimental setup

### Vacuum facility and thruster implementation

The thruster functionality test has been performed in the DLR facility, i.e., STG-MT. The chamber has dimensions of $\phi 1$ m × 1 m and an ultimate pressure of $3 \times 10^{-6}$ mbar. After successful functionality verification, the ALFVEN thruster is tested in the Mega-HPT facility at Tohoku University in Japan, including tests of ignition capability, RF circuit properties, thruster potential, and plume properties near the exit of the ALFVEN thruster. The gases for the experiment include argon 5.0 and krypton 5.0.

The dimension of the Mega-HPT chamber is ∅1 m × 2 m with an ultimate pressure around $1 \times 10^{-6}$ mbar. [18] The implementation of the thruster in Mega-HPT can be found in the Fig. 8. The thruster is electrically isolated from the ground of the facility. The power is transmitted from the RF power generator to ALFVEN through a coaxial cable and feedthrough. An RF isolator is adapted at the thruster's power inlet port to create electrical insulation for the DC component on the core and the shielding of the coaxial cable, but free transmission for the AC component. A high-frequency voltage probe, i.e., PMM 513 A from PMK GmbH, is connected to the shielding of the thruster to monitor the electric potential of the ALFVEN- 4050 during operation. The voltage probe is a 10:1 passive voltage sensor up to 300 V, which has a bandwidth of up to 250 MHz and an input impedance of $10M\Omega$ and rising time of 1.4 ns An oscilloscope monitors the attenuated voltage from the probe. The measurement duration is one second after receiving a TTL trigger from the RF power supply, which has a one-second delay after the RF power is forwarded to the ALFVEN thruster. The thruster potential recorded in this test campaign is an average of the voltage measurements.

### Measurement of RF circuit properties

The RF circuit properties of the ALVFEN thruster are monitored by an Octiv Poly 2.0 sensor between the power unit and the load. The sensing properties and their uncertainty at a center-frequency (CF) of 40.65 MHz is summarized in the Table 1.

### Measurement of plasma properties

A planar Langmuir probe is used to assess the plasma plume properties, where the electron temperature ($T_e$) and the ion saturation current ($I_{\rm is}$) are determined. The probe is

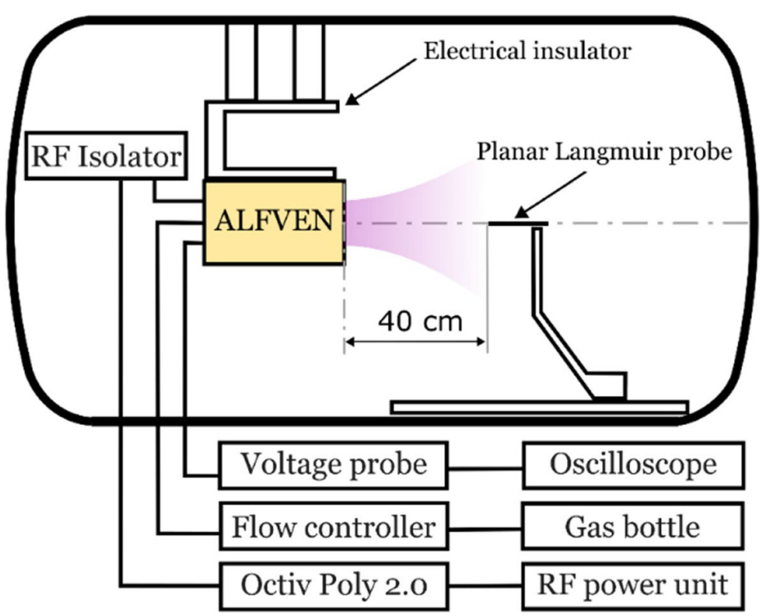


**Fig. 8** Implementation of ALFVEN- 4050 in MegaHPT at Tohoku University

**Table 1** Measurement range and uncertainty of Octiv Poly 2.0 from Impedans Ltd at 40.65 MHz

| Parameters | Value | Uncertainty |
|---|---|---|
| Frequency | 40.65 MHz (CF) ±2MHz | ±1kHz |
| Power | up to 12 kW | ±1% |
| Voltage | up to 1850 V | $1V_{rms}$ or ±1% |
| Current | up to 9 A | $0.1A_{rms}$ or ±1% |
| Impedance | $10^{-2}$ to $10^{4}\,\Omega$ | < 0.5% for the testing range |
| Phase | ±180° | ±1° |

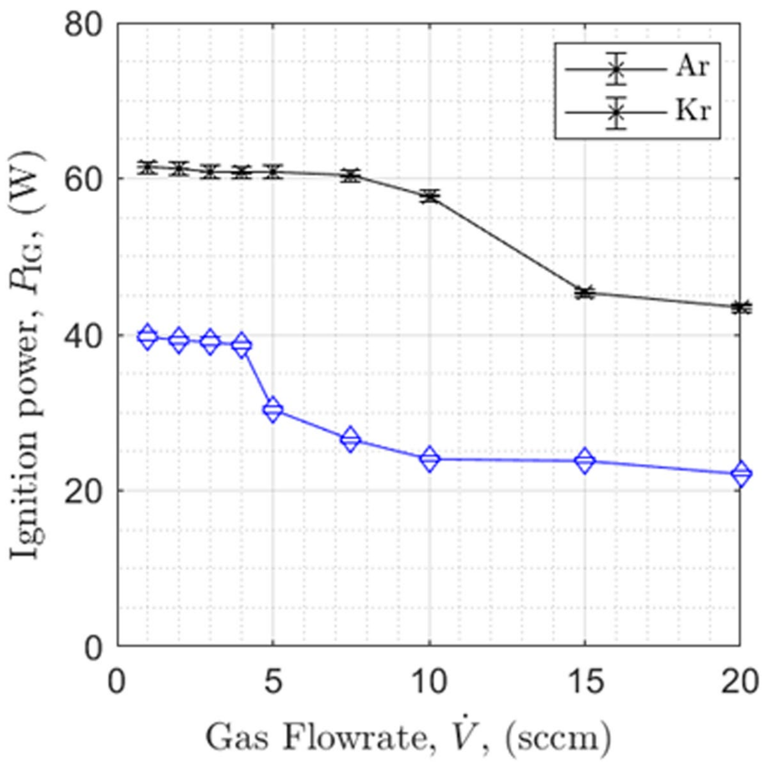


**Fig. 9** Assessment of ALFVEN- 4050 direct ignition capability. The test is performed without external assistance, such as an external electron source or gas shock

placed at 40 cm downstream from the ALFVEN thruster's exit to minimize RF wave interference from the thruster's antenna to the Langmuir probe. The detector has a 3-mm diameter, facing perpendicular to the thruster axis. The description of the Langmuir probe setup can be found in Ref. [19].

## Experimental result

### Ignition capability

The ignition capability of ALFVEN- 4050 with krypton and argon is shown in Fig. 9, respectively. The ignition test of ALVEN- 4050 is conducted without an extra assistance mechanism. Higher power is expected to achieve argon ignition owing to its higher ionization energy than krypton. The required ignition power is lower at a higher gas flow rate

($\dot{V}$), which suggests the higher collisional frequency of heavy particles could enhance the ignition of RF plasma. On the other hand, the ignition power remains almost constant when the thruster is operated below 5 sccm for krypton and 7.5 sccm for argon, suggesting that the collisional effect of heavy particles is negligible from the ignition. In addition, the tendency is inconsistent with the known Paschen discharge curve, where the lower pressure should yield a higher breakdown voltage. This also suggests an unexpected influence is dominating the ignition capability of the plasma when the $\dot{V}$ is low.

### Impedance variation

The circuit components change when plasma is present in the discharge chamber of the ALFVEN- 4050, which forms a secondary circuit by plasma interacting with the leg of SLA. The effect of the plasma on $Z_1$ is relatively minor since the $Z_1$ only represents a short compared to the leg's component. [16]. Therefore, the main impact of plasma on the electrical properties of SLA is through the interaction between the leg and plasma ($Z_2$). A schematic of the antenna leg and the secondary plasma circuit is summarized in Fig. 10. The plasma self-inductance and the resistance are represented by the $L_p$ and$R_p$, respectively. In addition to the plasma electrical properties, the mutual inductance between each leg and the plasma $M_{lp}$ also presents. An equivalent circuit when plasma is presented can be represented by a simple series circuit with the$Z_2'$, shown on the right of Fig. 10. $Z_2\prime$ can be written as$(R_{leg} + aR_p) + j\omega(L_{leg} - L_p - aR_p/\nu)$, where $a = \omega^2 M_{lp}^2/[\omega L_p + (R_p\omega/\nu)^2 + R_p^2]$ is the transformation factor. [16] The parameter $\omega$ and $\nu$ is the angular velocity at the frequency of RF input and effective electron collisional frequency. Although the electrical components can represent the circuit, the individual value of each component is hard to characterize since the $M_{lp}$ is not able to be quantified without knowing the $L_p$ and$R_p$, and the current distribution at each leg ($i_{leg}$). Nevertheless, the load impedance variation can show qualitative plasma properties under different operating conditions, providing insights into the plasma discharge characteristics.

The variation of the load impedance of the ALFVEN- 4050 in operation is summarized in Fig. 11. For both gases, the almost constant $Z_{real}$ at low $\dot{V}$ indicates that the impact from the presence of plasma is negligible, suggesting negligible $R_p$ and $L_p$. The $Z_{real}$ starts

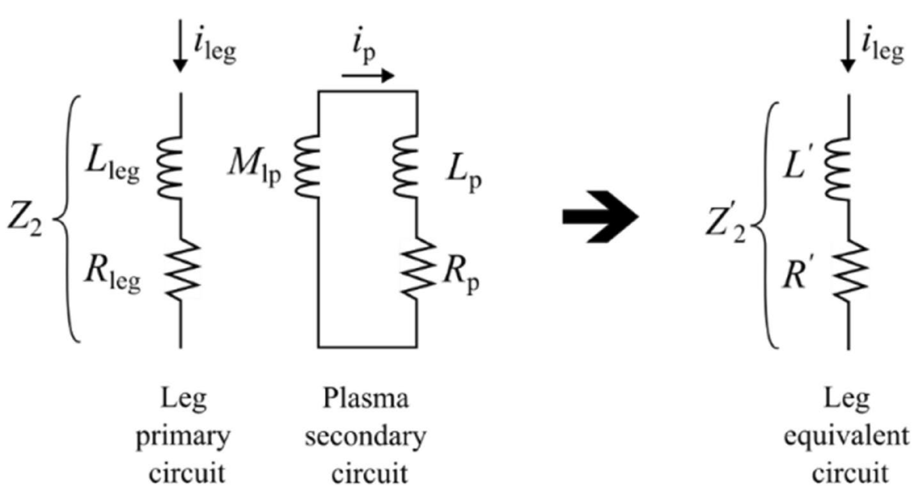


**Fig. 10** Equivalent circuit of SLA's leg when plasma presents in ALFVEN- 4050

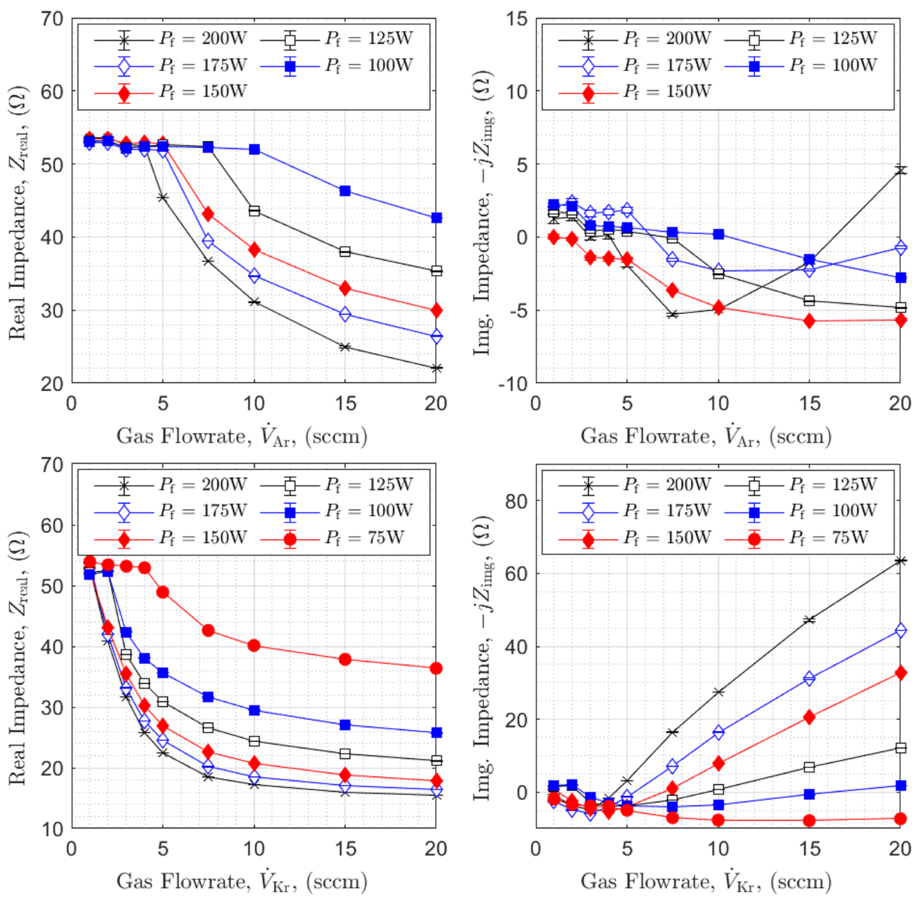


**Fig. 11** Load impedance variation of ALFVEN- 4050 at different argon (upper row) and krypton (lower row) gas flow rates $\dot{V}$ and RF forward power $P_\mathrm{f}$

decreasing when $\dot{V}$ is above a certain threshold, which indicates that the plasma in the discharge chamber gradually dominates the properties of the load circuit. The reduced $Z_\mathrm{real}$ indicates an enhanced conductivity in the overall load circuit with plasma, which hints at a much higher plasma density in the discharge chamber compared to the low $\dot{V}$ conditions. This trend is accompanied by the plasma density increase (i.e., see $I_\mathrm{is}$ measurement in Fig. 13). The increase of the plasma density is a result of higher electron-neutral collisional frequency by the increasing $\dot{V}$.

The threshold was reduced to a lower $\dot{V}$ as the $P_\mathrm{f}$ increased, where variation is more prominent in argon than in krypton. In addition, a lower $Z_\mathrm{real}$ is observed when tested with krypton than with argon at the same $\dot{V}$ and $P_\mathrm{f}$, suggesting a higher plasma density with krypton. This is related to the krypton feature of lower ionization energy and larger electron-impact ionization cross-section. The $Z_\mathrm{real}$ with krypton tends to saturate as the $\dot{V}$ increases, suggesting a saturation of the plasma density.

The $Z_\mathrm{img}$ also remain at a constant value at a lower $\dot{V}$ and start decreasing when $\dot{V}$ is above the threshold, the same as the observation in $Z_\mathrm{real}$ evolution. This observation suggests the plasma density might have a significant impact on the variation of $Z_\mathrm{img}$. A similar $Z_\mathrm{img}$ curve, e.g., krypton at $P_\mathrm{f} = 125\mathrm{W}$ verse argon at $P_\mathrm{f} = 200$ W, is observed in the cases with similar $Z_{\mathrm{real}}$ trend. This also suggests the variation of the $Z_{\mathrm{img}}$ might be dominated by the plasma density.

The negative $Z_{\mathrm{img}}$ indicates that the load becomes more of a capacitive-like circuit when plasma presents, while the positive $Z_{\mathrm{img}}$ indicates an inductive-like load. For both gases, the $Z_{\mathrm{img}}$ decreases slightly and starts to increase significantly as the $\dot{V}$ increases. This indicates that the capacitive discharge is easier to establish at a lower $\dot{V}$ or a lower $P_{\mathrm{f}}$.

In short, the appearance of plasma can provide a more prominent inductive influence in the load circuit at a higher $P_{\mathrm{f}}$, observed from the rapidly increasing $Z_{\mathrm{img}}$ of krypton when $\dot{V}$ increases. The dominated inductive characteristic of load also suggests that plasma behaves like an inductive component of the load circuit, as a transformer. This also hints at the fact that there is a high current flowing within plasma and creating inductive coupling with an antenna. Unlike krypton, argon plasma behaves more like a capacitive component to the load circuit in the given operational region. Yet, the dominance of the inductive characteristic can be observed at higher $P_{\mathrm{f}}$ or $\dot{V}$.

## Thruster potential

Plasma potential in the discharge chamber is an important indicator for the beam acceleration and electron temperature in the plume. By considering the sheath theory, the difference between plasma potential and the wall should remain a correlation as follows [20]:

$$\frac{\Delta V}{T_e} = \frac{V_p - V_0}{T_e} = \frac{1}{2}\left[1 + \ln(\frac{M_i}{2\pi m_e})\right] \tag{1}$$

, where the $V_p$ represents the bulk plasma potential and $V_0$ is the reference potential, while $M_i$ represent the mass of ion species and $m_e$ is the electron mass. The measurement of the ambipolar acceleration and electron kinetics shown in an ECR thruster with magnetic nozzle indicated that the plasma potential follows the given correlation quite well. [21]

Since ALFVEN- 4050 is electrically isolated from the ground, the plasma and thruster body can reach the electric potential balance during the thruster's operation due to the contact of plasma with the distributing plate, which serves as a floating probe to measure the plasma potential in the discharge chamber. Accordingly, measuring the potential from the thruster's shielding can monitor the plasma potential. The measurement location is on the quartz-tube cap, which is in contact with the distributed plate and the thruster body, via a shielded high-voltage cable to the high-frequency voltage probe in ambient.

The thruster potential $V_{\mathrm{Thr}}$ is monitored with a high-frequency voltage probe and oscilloscope, summarized in Fig. 12. The high-frequency components at the operating frequency can be observed in the $V_{\mathrm{Thr}}$ measurement, but its amplitude is relatively small compared to the DC component. Accordingly, the discussion here focuses only on the DC voltage.

The $V_{\mathrm{Thr}}$ increased exponentially as $\dot{V}_{\mathrm{Kr}}$ reduced below 5 sccm, indicating high plasma potential and suggesting a high $T_e$ appears in the discharge chamber of ALFVEN- 4050. This behavior is also identified via measuring the $T_e$ in the plume (see later in Fig. 13). One explanation could be the insufficient depletion of electron kinetic energy due to limited electron-neutral collision at a low $\dot{V}$. On the other hand, it also suggests very

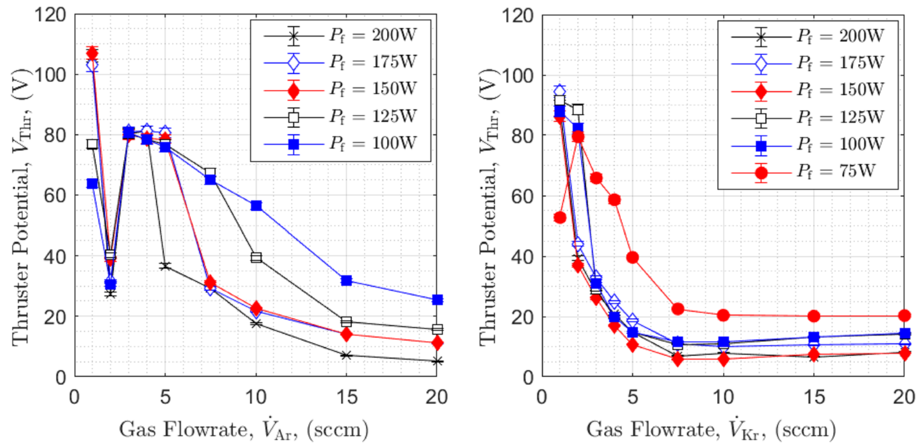


**Fig. 12** Thruster potential variation of ALFVEN- 4050 at different argon (left) and krypton (right) gas flow rates $\dot{V}$ and RF forward power $P_{\mathrm{f}}$

efficient energy transmission from the antenna to the electrons at the low $\dot{V}$. The evolutions of $V_{\mathrm{Thr}}$ at different $P_{\mathrm{f}}$ seem to be saturated at specific values when $\dot{V}_{\mathrm{Kr}} \geq 5\mathrm{sccm}$, suggesting a saturation of the $T_e$ in the discharge chamber. This trend is also observed in the $T_e$ measurement in the plume. (see later in Fig. 13).

A similar $V_{\mathrm{Thr}}$ tendency to the $\dot{V}$ is also observed for argon, where the $V_{\mathrm{Thr}}$ seems to change at the same condition with the reduction of $Z_{\mathrm{real}}$ (see also in Fig. 11). The $V_{\mathrm{Thr}}$ in argon are generally higher than in krypton at the same $\dot{V}$ and same $P_{\mathrm{f}}$, suggesting a higher $T_e$ in the discharge chamber. The discharge with argon has a comparably limited depletion of electron kinetic energy in the ionization processes compared to krypton due to the feature of the gas species, i.e., argon has higher ionization energy and smaller electron-impact ionization cross-section in general. Interestingly, the lower $P_{\mathrm{f}}$ tends to yield a higher $V_{\mathrm{Thr}}$ at the same $\dot{V}_{\mathrm{Ar}}$, which is only observed in krypton's condition at $P_{\mathrm{f}} = 75\mathrm{W}$. This suggests the appearance of the capacitive coupled plasma. In addition, the analogy between argon's conditions and krypton's conditions at $P_{\mathrm{f}} = 75\mathrm{W}$ are the dominant capacitive characteristics of the load circuit, shown in the $Z_{\mathrm{img}}$ of Fig. 11. As soon as the inductive component starts dominating the load circuit properties, the $V_{\mathrm{Thr}}$ decreases significantly as the krypton cases.

One point worth mentioning is the significant $V_{\mathrm{Thr}}$ drop occurred explicitly at the $\dot{V} = 2$ sccm argon, regardless of the value of $P_{\mathrm{f}}$. No abnormality is observed in the load impedance measurement. This phenomenon can be repeatedly reproduced at different $P_{\mathrm{f}}$, which hints at a unique unknown mechanism that dominated the discharge.

## Plasma properties

The plasma properties near the exit of the ALFVEN- 4050 are summarized in Fig. <div class="oxe_ins">13</div><div class="oxe_del">1</div><div class="oxe_del">2</div>. The evolution of the $I_{\mathrm{is}}$ is very similar to the evolution of $Z_{\mathrm{real}}$, supporting the argument that the increase in conductivity when $\dot{V}$ and $P_{\mathrm{f}}$ increased is owing to the rise of the plasma density. A significant $I_{\mathrm{is}}$ jump can be observed in argon plasma when the $Z_{\mathrm{real}}$ starts to decrease, suggesting a condition where plasma conductivity significantly increases. This $I_{\mathrm{is}}$ jump could be the indication of the E–H mode transition or the H-W

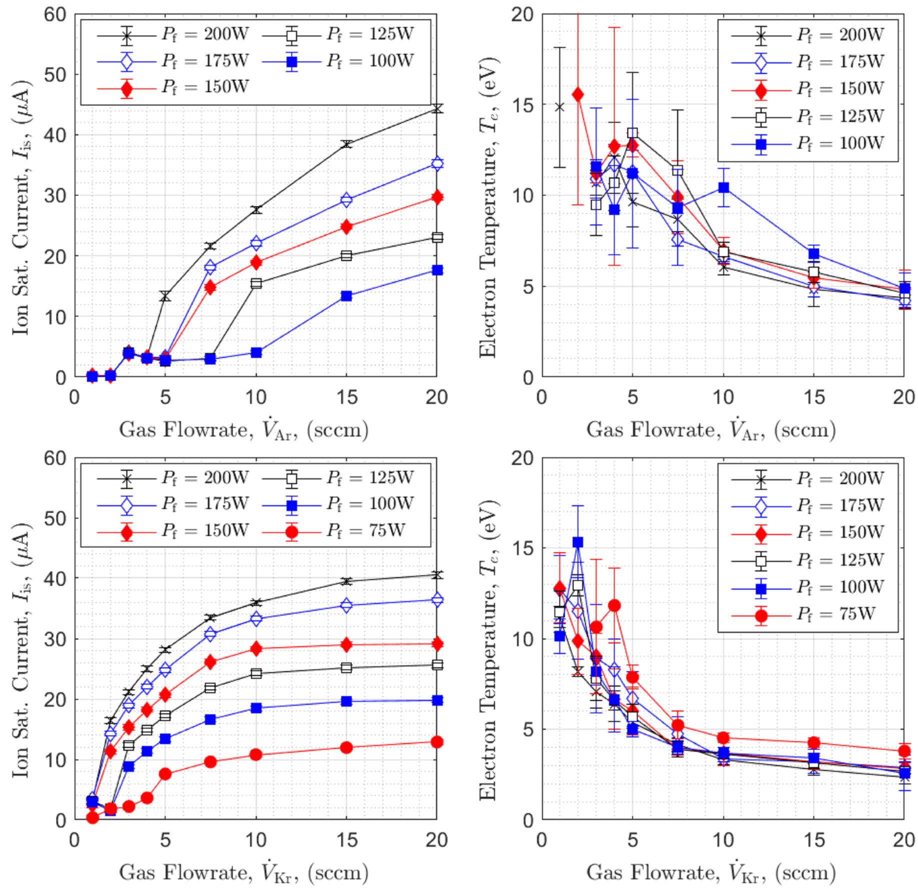


**Fig. 13** Ion saturation current $I_{\mathrm{is}}$ variation of ALFVEN- 4050 at different argon (upper row) and krypton (lower row) gas flow rates $\dot{V}$ and RF forward power $P_{\mathrm{f}}$

transition. It can not be confirmed which transition is triggered without measuring the whistler wave. On the other hand, no significant $I_{\mathrm{is}}$ jump can be clearly identified from krypton plasma, which is possible when the plasma source is operated at a high frequency. In addition, the $I_{\mathrm{is}}$ in the krypton plume reaches to a saturated value at high $\dot{V}_{\mathrm{Kr}}$, but this is not observed in the argon plume. The trend of argon $I_{\mathrm{is}}$ (also in the $Z_{\mathrm{real}}$ in Fig. 11) suggests that a higher $P_{\mathrm{f}}$ or $\dot{V}_{\mathrm{Ar}}$ is required to reach the saturation of $I_{\mathrm{is}}$ as in krypton.

The $T_e$ appears relatively insensitive to $P_{\mathrm{f}}$. The $T_e$ in krypton's conditions reduces rapidly when $\dot{V}$ increases from a lower value. With the significant growth of $I_{\mathrm{is}}$, one can conclude that the reduced $T_e$ is the outcome of the electron kinetic energy depletion driven by the increase of electron-neutral collisional frequency. On the other hand, the $T_e$ in argon conditions shows a relatively mild decreasing tendency to the increasing $\dot{V}$, suggesting a less effective ionization process than the krypton, possibly due to the difference in the electron-impact collisional cross-section. In general, the significantly lower $T_e$ at high $\dot{V}$ can be attributed to the significant depletion of the electron kinetic energy to the plasma generation or a less effective coupling of the RF energy to the plasma due to the drifting of $Z_{\mathrm{load}}$ away from the 50Ω. This requires further experiments to clarify the cause.

Unfortunately, the Langmuir probe measurement for the condition of $\dot{V}_{\mathrm{Ar}} = 2$ sccm is too noisy to yield a reasonably accurate $T_e$. Yet, this also indicates an unknown mechanism existed in the plasma discharge processes at the given condition.

### Estimated ionization rate coefficient

By further estimating the ionization rate coefficient, one could evaluate the ionization behavior with the variation of the $V_{\mathrm{Thr}}$. The equation used for the ionization rate coefficient $k_{\mathrm{ion}}$ is shown as follows:

$$k_{\mathrm{ion}} = \langle \sigma_{\mathrm{ion}} \nu \rangle = \int_0^\infty \sigma_{\mathrm{ion}}(\epsilon)\, \epsilon^{1/2} f_{\mathrm{EEDF}}(\epsilon)\, d\epsilon \quad (2)$$

, where$\sigma_{\mathrm{ion}}$ is the electron impact ionization cross-section, $\epsilon$ is the impact energy in a unit of eV, $f_{\mathrm{EEDF}}$ is the electron energy distribution function (EEDF). The used ionization cross-section for argon and krypton in this paper is listed in the Ref. [22, 23] The Maxwellian EEDF is assumed for the calculation, which can be written as follows:

$$f_{\mathrm{EEDF}} = \frac{2}{\sqrt{\pi}}\, T_e^{-3/2}\, \epsilon^{1/2}\, e^{-\epsilon/T_e} \quad (3)$$

, where the $T_e$ is in the unit of eV. The EEDF within the discharge chamber can be calculated from the $T_e$ of the plume by assuming the plasma undergoes isothermal expansion. The ionization rate can then be determined by $dN_{\mathrm{ion}}/dt = k_{\mathrm{ion}} n_n n_e$. Although, the $n_n$ within the discharge chamber can be calculated from the vacuum chamber pressure under the ideal gas assumption; the $n_e$ in the discharge chamber can not be determined with the given measurement result. Nevertheless, a $n_e^{-1} dN_{\mathrm{ion}}/dt = k_{\mathrm{ion}} n_n$ can still qualitatively represent the ionization rate. The result of $k_{\mathrm{ion}}$ and $k_{\mathrm{ion}} n_n$ is plotted in the Fig. 14. One can see the ionization rates for argon and krypton are much higher at a gas flow rate below 4 sccm, which suggests efficient energy coupling from the antenna to plasma discharge and hints at the optimization of $\widetilde{E} \times \overrightarrow{B_0}$ effect in the ALFVEN thruster. As soon as the flow rate increases, the ionization rate of both gases becomes much lower, suggesting damping on $\widetilde{E} \times \overrightarrow{B_0}$ effect generated by the antenna. However, the observation of increasing $i_{\mathrm{is}}$ in Fig. 13 with the gas flow rate indicates the continuously increasing plasma density even when the ionization rate is significantly reduced. Thus, it hints that the ionization processes at higher flow rate conditions are dominated by the increase of particle density instead of the ionization rate coefficient. From the plots of $k_{\mathrm{ion}} n_n$, the inclusion of the neutral particle density could be a better representation for the discussion of the ionization rate. For cases in argon, the highest value of $k_{\mathrm{ion,\,Ar}} n_{\mathrm{Ar}}$ does not appear at the same flow rate condition as in the $k_{\mathrm{ion}}$ values. In addition, the maximum value at each power level changes depending on a neutral density threshold. This suggests that the density of argon particles below the threshold condition significantly affects the ion production rate. On the other hand, the value of $k_{\mathrm{ion,\,Kr}} n_{\mathrm{Kr}}$ for krypton cases remain similar to the figure shown with $k_{\mathrm{ion,\,Kr}}$, which suggests the ion production rate is less sensitive to the krypton particle density, owing to its larger ionization cross-section and low ionization energy threshold than argon. An interesting correlation can be found by comparing the $k_{\mathrm{ion,\,Ar}} n_{\mathrm{Ar}}$ with the $V_{\mathrm{Thr}}$ shown in Fig. 12 when testing with argon. The decrease in the $V_{\mathrm{Thr}}$ become most significant when the operating flow rate is higher than the threshold condition shown in the $k_{\mathrm{ion,Ar}} n_{\mathrm{Ar}}$. This indicates that the ion production process slowly takes over by the boost of the swarm electron density, which can also be supported by the $I_{\mathrm{is}}$ measurement in Fig. 13. On the other hand, the

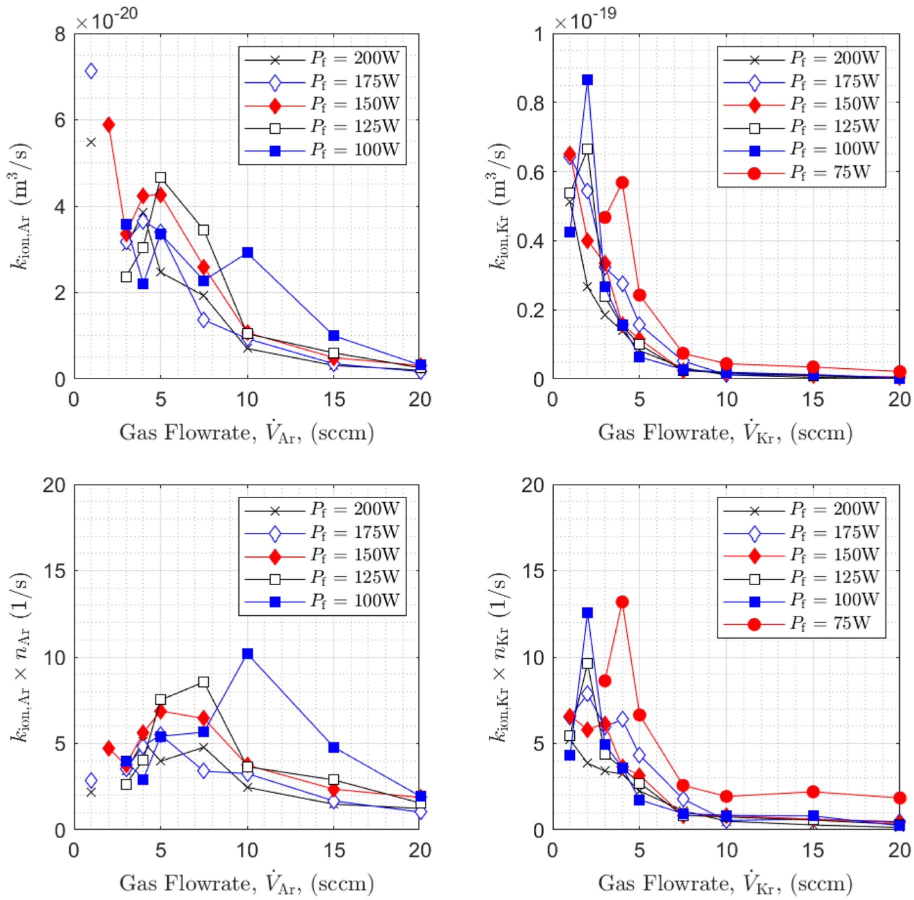


**Fig. 14** Estimated ionization rate coefficient $k_{\mathrm{ion}}$(upper row) and normalized ionization rate $k_{\mathrm{ion}}n_n$ (lower row) of ALFVEN- 4050 at different argon and krypton gas flow rates $\dot{V}$ and RF forward power $P_{\mathrm{f}}$

peak $k_{\mathrm{ion,Kr}}n_{\mathrm{Kr}}$ values at all levels of $P_{\mathrm{f}}$ appears at a relatively low flow gas rate condition, which also aligned with cases observed with high $V_{\mathrm{Thr}}$. Significantly reduction of the $V_{\mathrm{Thr}}$ also appears at higher gas flow rate conditions, where swarm electrons dominate the ion production processes.

The $k_{\mathrm{ion,\,Ar}}n_{\mathrm{Ar}}$ also demonstrate an interesting correlation with $Z_{\mathrm{real}}$ and $Z_{\mathrm{img}}$ shown in Fig. 11. A significant decrease of the $Z_{\mathrm{real}}$ appears at the same flow rate conditions where ionization processes are dominated by swarm electrons, supporting the statement of enhancing plasma conductivity. The same statement applies well to the impedance variation when operating with krypton. The high $k_{\mathrm{ion}}$ appears when the $Z_{\mathrm{img}}$ of the load circuit appears with the capacitive components, while the presence of swarm electrons appears when the inductive components show in the $Z_{\mathrm{img}}$ of the load circuit. The ionization processes at the conditions with high $k_{\mathrm{ion}}$ are driven by the $\widetilde{E}$, which leads to the optimization of $\widetilde{E} \times \overrightarrow{B}_0$ product, as discussed in the previous paragraph. On the other hand, the presence of the inductive component in $Z_{\mathrm{img}}$ suggests that swarm electrons could transform an ideal load circuit into an inductor. This transformation is also accompanied by the damping of the $\widetilde{E} \times \overrightarrow{B}_0$ effect, leading to a lower $k_{\mathrm{ion}}$.

## Conclusion

The ALFVEN thruster, i.e., an RF plasma thruster with an SLA, works towards optimizing the wave-plasma coupling mechanism by achieving orthogonality of the steady applied magnetic field along the discharge chamber and an oscillating linear-polarized electromagnetic field in the transverse direction of the discharge chamber. The presented ALDVEN- 4050 is designed at a specifically resonant frequency with an antenna impedance of 50Ω. This allows a more distinguishable evaluation of the variation of overall load impedance when plasma presents thruster operation. Both steady magnetic and electromagnetic fields have been verified by experiments or via 3D simulation to ensure the working principle of the ALFVEN thruster.

The direct ignition capability of the ALFVEN thruster demonstrates a promising performance feature for an RF plasma source by optimizing the arrangement of the electromagnetic wave generated by the antenna and the steady magnetic field provided by the magnetic optics. Despite this work not detailing the electric circuit properties of the load from the impedance measurement, owing to the feature of the complicated circuit between antenna and plasma, the variation of the load impedance for ALFVEN- 4050 still provides a clear correlation of the load impedance to the plasma plume properties at different thruster operating condition due to antenna characteristics.

At low $\dot{V}$ conditions, the almost unchanged load impedance indicates that the add-on electrical components from plasma are negligible. Meanwhile, the high $V_{\mathrm{Thr}}$ and the $T_e$ of the plume at the given conditions indicates a high $T_e$ in the discharge chamber of ALFVEN- 4050, which is evidence of the effective energy transmission from the antenna to the plasma.

The impact of plasma on the $Z_{\mathrm{load}}$ is discussed by $Z_{\mathrm{real}}$ and $Z_{\mathrm{img}}$ individually. From the discussion of $Z_{\mathrm{real}}$ evolution, the load circuit's conductivity increases, providing a higher electron-neutral collisional frequency in the discharge chamber, leading to enhanced plasma density. In addition, krypton can achieve a higher conductivity at the same given $P_{\mathrm{f}}$ and $\dot{V}$, suggesting a higher plasma density in krypton than in argon plasma in general. This is related to the krypton feature of lower ionization energy and larger electron-impact ionization cross-section.

From the discussion of $Z_{\mathrm{img}}$ evolution, a clear trend of the capacitive-like and inductive-like load can be identified at different operating conditions of the ALFVEN- 4050 by observing the variation of $Z_{\mathrm{img}}$. The results suggest that the plasma density might have a significant impact on the variation of $Z_{\mathrm{img}}$. The mild transient from the capacitive-like load to the inductive-like load is observed at a certain $\dot{V}$ or a particular input RF power, suggesting the existence of the mode transition in plasma. In addition, the transition occurs at a much lower $\dot{V}$ when ALFVEN- 4050 is operated with krypton than with argon. This also suggests the importance of the plasma density in the discharge chamber to the $Z_{\mathrm{img}}$.

The measurement of the $V_{\mathrm{Thr}}$ provides more insights into plasma discharge. The $V_{\mathrm{Thr}}$ also shows a similar evolution trend to the $Z_{\mathrm{real}}$, suggesting a strong correlation to the plasma density in the discharge chamber. The high $V_{\mathrm{Thr}}$ at the low $\dot{V}$ demonstrates a high $T_e$ inside the discharge chamber. On the one hand, it results from the insufficient depletion of electron kinetic energy due to limited electron-neutral collision. On the other hand, high $V_{\mathrm{Thr}}$ in the discharge chamber also indicates the effective energy transmission from the antenna to the plasma, even at a low ionization degree. A higher $V_{\mathrm{Thr}}$ is generally observed with a lower $P_{\mathrm{f}}$ regardless of the operating gases, suggesting the appearance of the capacitive coupled plasma. Nevertheless, the significantly reduced $V_{\mathrm{Thr}}$ is identified when the inductive component starts dominating the load circuit properties. Yet, significant $V_{\mathrm{Thr}}$ drop is observed specifically at $\dot{V} = 2$ sccm argon hints at a unique unknown mechanism that dominated the discharge.

In both argon and krypton, the evolution of the plume $I_{\mathrm{is}}$ provides qualitative evidence to support the discussion of plasma density evolution within the discharge chamber. A jump in plasma density can be identified in the argon plume, but it can not be confirmed if the jump results from the E–H mode transition or the H-W transition. On the other hand, the jump of krypton plume density is not so distinguishable as the condition in argon at a low $\dot{V}$, suggesting that the krypton can achieve a much more efficient energy coupling to the ionization processes even with a limited electron-neutral collision condition.

The evolution of the plume $T_e$ the trend is relatively independent of the $P_{\mathrm{f}}$, but strongly dominated by the $\dot{V}$, suggesting that the energy transmission from the antenna to the plasma is strongly dominated by the electron-neutral collisional frequency instead of the electrical component of the antenna.

Further extended discussion on the ionization rate coefficient $k_{\mathrm{ion}}$ reveals more details in the discharge behavior. A high $k_{\mathrm{ion}}$ at a low gas flow rate condition suggests the effective power coupling from antenna to plasma, owning to optimization of $\widetilde{E} \times \overrightarrow{B}_0$ product. As the flow rate increases, plasma density rises despite lower $k_{\mathrm{ion}}$, indicating that ionization at higher flow rates is primarily driven by increased particle density rather than the ionization rate coefficient. It also suggests that the increased collision frequency would cause the deterioration of the $\widetilde{E} \times \overrightarrow{B}_0$ product. Above a certain gas flow rate threshold, the ionization process is then dominated by swarm electrons, which can be detected by observing the lower $Z_{\mathrm{real}}$ and the inductive component in the $Z_{\mathrm{img}}$. This hints that swarm electron plays a crucial role in swarm electrons play a crucial role in the discharge of the ALFVEN thruster, ultimately affecting the thruster's performance and its electrical characteristics.

In summary, optimizing the performance of an electrodeless plasma thruster is crucial. The ALFVEN concept offers the possibility to optimize the discharge performance from theory and from an engineering perspective, i.e., optimizing the $\widetilde{\mathrm{E}} \times \overrightarrow{B}_0$ product and using RF to achieve low loss in the power system and transmission line. The promising ignition capability of the ALFVEN thruster offers a promising solution for the next-generation EP concept to overcome the low mass utilization issue in low-power RF plasma thrusters and to enable the possibility of optimizing the acceleration performance of magnetic nozzles. This feature can offer a more extensive operation range for the RF thruster and extend its applicability in different missions and environments.

**Acknowledgements**
This work is partially support by the Bilateral Collaborations between the German Academic Exchange Service (Grant No. 57709927) and the Japan Society for the Promotion of Science (Grant No. 120243502).

**Authors' contributions**
The ALFVEN thruster and the RF power transmission/measurement circuit from the thruster to the RF power system were designed and manufactured by Y.A.C. at the German Aerospace Center (DLR). C.G. provided technical support on antenna manufacturing. Y.A.C. performed the simulation and measurement of the magnetic field and s11 parameters. The vacuum chamber, RF power system, and Langmuir probe setup were provided by K.T. at Tohoku University. The RF sensors were provided by Y.A.C. from DLR. The discharge experiment and plasma plume measurement were performed by Y.A.C. and K.T. together. The transportation of the thruster between DLR and Tohoku University proceeded by the Y.A.C., M.G., and K.T. C.G. supported the implementation of the experiment at Tohoku University. The data acquisition, analysis, and discussion were proceeded by Y.A.C and K.T. The first draft written by Y.A.C. is reviewed and revised by all the authors.

**Funding**
Open Access funding enabled and organized by Projekt DEAL. DAAD/JSPS Bilateral Joint Research Project,57709927,Deutsches Zentrum für Luft- und Raumfahrt,DEEP,DEEP,DEEP,Japan Society for the Promotion of Science,120243502

**Data availability**
The data that support the findings of this study are available from the corresponding author upon reasonable request.

## Declarations

**Competing interests**
The authors declare no competing interests.

Received: 19 December 2024 Accepted: 21 March 2025
Published online: 14 April 2025

**References**

1. Mazouffre S (2016) Electric propulsion for satellites and spacecraft: established technologies and novel approaches. Plasma Sources Sci Technol 25(3):033002. https://doi.org/10.1088/0963-0252/25/3/033002
2. Sheppard AJ, Little JM (2022) Performance analysis of an electron cyclotron resonance thruster with various propellants. J Propul Power 38(6):998–1008. https://doi.org/10.2514/1.B38698
3. Bellomo N et al (2022) Design and in-orbit demonstration of REGULUS, an iodine electric propulsion system. CEAS Space J 14(1):79–90. https://doi.org/10.1007/s12567-021-00374-4
4. Takahashi K (2022) Thirty percent conversion efficiency from radiofrequency power to thrust energy in a magnetic nozzle plasma thruster. Sci Rep 12(1):18618. https://doi.org/10.1038/s41598-022-22789-7
5. Takahashi K, Takao Y, Ando A (2016) Neutral-depletion-induced axially asymmetric density in a helicon source and imparted thrust. Appl Phys Lett 108(7):074103. https://doi.org/10.1063/1.4942469
6. Takahashi K, Charles C, Boswell RW (2013) Approaching the theoretical limit of diamagnetic-induced momentum in a rapidly diverging magnetic nozzle. Phys Rev Lett 110(19):1–5. https://doi.org/10.1103/PhysRevLett.110.195003
7. Ruiz M et al (Jun.2022) "Results of the first Helicon Plasma Thruster (HPT) coupling test campaign within the HIPATIA project", in *37th International Electric Propulsion Conference*. MA, USA, Cambridge.
8. Takahashi K, Sugawara T, Ando A (2020) Spatially- and vector-resolved momentum flux lost to a wall in a magnetic nozzle rf plasma thruster. Sci Rep 10(1):1061. https://doi.org/10.1038/s41598-020-58022-6
9. Chan Y-A, Herdrich G (2023) Design criteria assessment of a magnetic nozzle. Phys Scr 99(1):015608. https://doi.org/10.1088/1402-4896/ad15d4
10. Romano F et al (2020) RF helicon-based inductive plasma thruster (IPT) design for an atmosphere-breathing electric propulsion system (ABEP). Acta Astronaut 176:476–483. https://doi.org/10.1016/j.actaastro.2020.07.008
11. F Romano, YA Chan, G Herdrich, Fasoulas S (2024) "Plasma Thruster with Birdcage Antenna," U.S. Patent 12 140 126 B2
12. Guittienne P, Jacquier R, Pouradier Duteil B, Howling AA, Agnello R, Furno I (2021) Helicon wave plasma generated by a resonant birdcage antenna: magnetic field measurements and analysis in the RAID linear device. Plasma Sources Sci Technol 30(7):075023. https://doi.org/10.1088/1361-6595/ac0da3
13. Kim JH, Hong YH, Chung CW (2019) High efficient plasma generation in an inductively coupled plasma using a passive resonant antenna. Plasma Sources Sci Technol 28(10):105018. https://doi.org/10.1088/1361-6595/ab496d
14. Kim JH, Chung CW (2022) Plasma and electrical characteristics depending on an antenna position in an inductively coupled plasma with a passive resonant antenna. Plasma Sources Sci Technol 31(1):015002. https://doi.org/10.1088/1361-6595/ac4146
15. Vinci AE, Mazouffre S (2023) Enhanced electron heating in the magnetic nozzle of a radio-frequency plasma via electron cyclotron resonance. EPL 141(4):44002. https://doi.org/10.1209/0295-5075/acb967
16. Guittienne P, Howling AA, Hollenstein C (2014) Analysis of resonant planar dissipative network antennas for rf inductively coupled plasma sources. Plasma Sources Sci Technol 23(1):015006. https://doi.org/10.1088/0963-0252/23/1/015006
17. Takahashi K, Hanaoka K, Ando A (2020) Fast and automatic control of a frequency-tuned radiofrequency plasma source. Front Phys 7:227. https://doi.org/10.3389/fphy.2019.00227
18. Takahashi K, Sumikawa S (2023) Experimental investigation on magnetic field strength providing thrust saturation in a magnetic nozzle radiofrequency plasma thruster. Plasma Phys Controlled Fusion 66(1):015012. https://doi.org/10.1088/1361-6587/ad1124

19. Takahashi K (2023) Comparison of vacuum-immersed helicon thrusters terminated by upstream magnetic and physical walls. J Phys D Appl Phys 56(47):475207. https://doi.org/10.1088/1361-6463/acef36
20. Lieberman MA, Lichtenberg AJ (2005) Principles of Plasma Discharges and Materials Processing, Wiley, New Jersey
21. Lafleur T, Cannat F, Jarrige J, Elias PQ, Packan D (2015) Electron dynamics and ion acceleration in expanding-plasma thrusters. Plasma Sources Sci Technol 24(6):065013. https://doi.org/10.1088/0963-0252/24/6/065013
22. Hayashi M (2003) Bibliography of electron and photon cross sections with atoms and molecules published in the 20th century Argon. National Institute for Fusion Science, Japan. Available: http://inis.iaea.org/search/search.aspx?orig_q=RN:34071469
23. S. Biagi, "Magboltz - transport of electrons in gas mixtures - Krypton cross-section." Sep. 25, 2011. [Online]. Available: https://magboltz.web.cern.ch/magboltz/.

## Publisher's Note